ACS APPLIED MATERIALS & INTERFACES

www.acsami.org

Research Article

Impedance-Based Nanoporous Anodized Alumina/ITO Platforms for Label-Free Biosensors

Sivaranjani Devarakonda, Baskar Ganapathysubramanian,* and Pranav Shrotriya*

Cite This: *ACS Appl. Mater. Interfaces* 2022, 14, 150−158

Read Online

ACCESS | Metrics & More | Article Recommendations | Supporting Information

ABSTRACT: We report an experimental and computational approach for the fabrication and characterization of a highly sensitive and responsive label-free biosensor that does not require the presence of redox couples in electrolytes for sensitive electrochemical detection. The sensor is based on an aptamer-functionalized transparent electrode composed of nanoporous anodized alumina (NAA) grown on indium tin oxide (ITO)-covered glass. Electrochemical impedance changes in a thrombin binding aptamer (TBA)-functionalized NAA/ITO/glass electrode due to specific binding of α-thrombin are monitored for protein detection. The aptamer-functionalized electrode enables sensitive and specific thrombin protein detection with a detection limit of ∼10 pM and a high signal-to-noise ratio. The transient impedance of the alumina film-covered surface is computed using a computational electrochemical impedance spectroscopy (EIS) approach and compared to experimental observations to identify the dominant mechanisms underlying the sensor response. The computational and experimental results indicate that the sensing response is due to the modified ionic transport under the combined influence of steric hindrance and surface charge modification due to ligand/receptor binding between α-thrombin and the aptamer-covered alumina film. These results suggest that alumina film-covered electrodes utilize both steric and charge modulation for sensing, leading to tremendous improvement in the sensitivity and signal-to-noise ratio. The film configuration is amenable for miniaturization and can be readily incorporated into existing portable sensing systems.

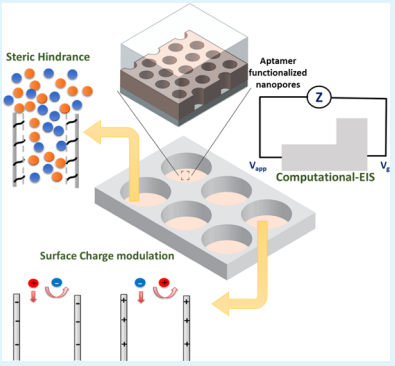

KEYWORDS: *nanoporous alumina, anodization, computational electrochemical impedance spectroscopy (EIS), label-free, aptasensor, sensing mechanism*

1. INTRODUCTION

Materials with nanopores and nanochannels are attractive for developing sensitive biosensor platforms because modifications in the surface and geometric properties of the pores are transduced to changes in ionic and mass transport.[1−3] Solid-state single nanopore-based electrochemical sensors can achieve high sensitivity and specific performance.[4,5] However, the fabrication of a single nanopore requires sophisticated nano/microfabrication techniques, which can be very cost-intensive. Nanoporous anodic alumina (NAA) films consisting of regular arrays of high-aspect-ratio nanochannels provide an excellent substrate for tunable biosensors. Nanochannel arrays in alumina can be fabricated with a wide range of geometrical attributes through the control of anodization parameters, and the fabricated nanochannnels are amenable to a range of functionalization.[6,7] In addition, fabrication of NAA arrays as thin films on a range of substrates including glass,[8] silicon,[9] PET,[10] and metals[11] enables easy integration into miniaturized, flexible, and portable sensing platforms. Transparent glass with an indium tin oxide (ITO) coating is an ideal substrate material choice, as many optical and electrochemical biosensors[12,13] require transparent and conductive substrates.

Architectures of electrochemical nanoporous biosensors can be designed to enhance sensitivity and selectivity by altering the diameter, shape, regions of functionalization, type of receptor, ionic conductivity, and electrolyte pH.[14−16] Conical and asymmetrically charged nanopores give rise to diode behavior showing nonlinear $I-V$ characteristics, and the degree of rectification is used as the sensing response to detect targets of interest.[17−19] Li et al.[20] studied the effect of regional functionalization on the ionic currents across asymmetric nanopores, reporting that the configuration where both outer and inner surfaces of the nanopores are functionalized provides the maximum response to the target. Vlassiouk et al.[21] reported steric effects due to DNA hybridization in uniformly functionalized nanopores, causing an increase in impedance in 20 nm diameter nanopores and no change in impedance for 200 nm pores.

Most of the previous studies reported on NAA biosensors identify either (i) steric hindrance[22,23] or (ii) charge modulation in nanopores[24] as the mechanism to detect the

Received: September 7, 2021
Accepted: December 2, 2021
Published: December 22, 2021

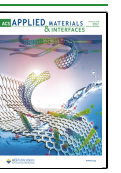

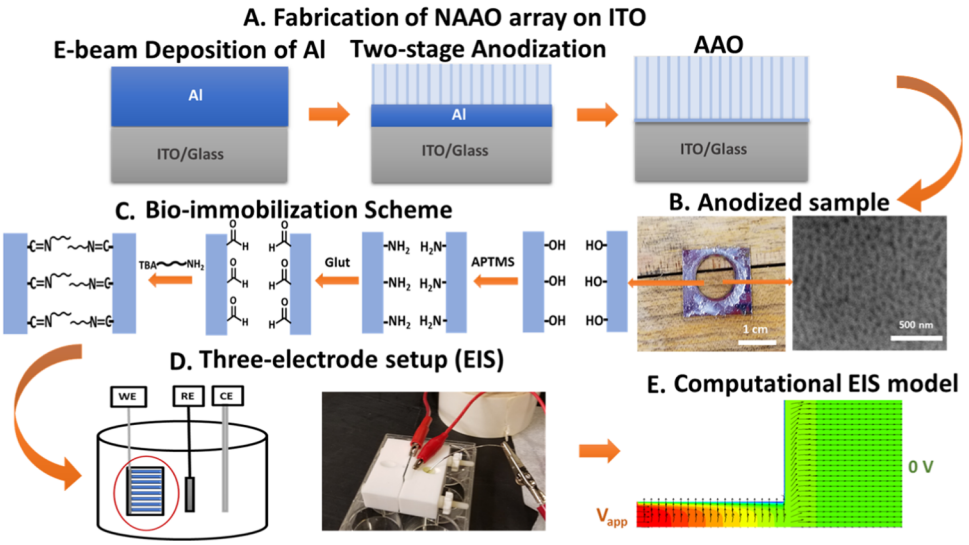

Figure 1. (A) Schematic of the fabrication of the NAA/ITO/glass sensing platform. (B) Picture of the anodized sample. (C) Attachment of TBA to NAA. (D) Electrochemical sensing method. (E) Computational EIS nanopore model.

target analyte. The mechanism governing the modification of ionic and mass transport upon binding strongly depends on the properties of the nanopores and the sensing configuration employed to construct the biosensor. We have previously reported the ability of the aptamer-functionalized gold-coated nanoporous alumina sensors for the detection of thrombin in the presence of high concentrations of human serum albumin.[25] The malleability and stability of aptamers ensured that the sensors could be reused seven times without compromising sensor performance.[25] Modification in ionic and mass transport is experimentally monitored using electrochemical impedance spectroscopy (EIS)[25] and the magnitude of impedance changes are correlated to the analyte concentration.

We report the fabrication and characterization of a biosensor consisting of NAA arrays grown on a conductive ITO/glass electrode using a two-stage anodization method. The nanopores are functionalized uniformly with a thrombin aptamer (TBA) to detect the α-thrombin protein. Transient ionic transport under a step voltage change for this sensor configuration is modeled using "computational EIS" to determine the impedance changes and quantitatively unravel the impact of various mechanisms governing the sensing response. The overview of the fabrication process, bioimmobilization, electrochemical sensing, and theoretical modeling is shown in Figure 1. The fabricated sensor format enables the ease of fabrication, cost-effectiveness, and ability to be miniaturized. The sensor response for label-free detection of thrombin is compared to previously reported sensors to demonstrate the efficacy of the sensor substrate. The measured and predicted impedance changes are compared to identify the mechanism governing the high specific response measure on NAA/ITO/glass substrates.

2. RESULTS AND DISCUSSION

2.1. Fabrication and Characterization of NAA/ITO/Glass. Regular nanoporous anodized alumina films were grown on ITO/glass using two-stage anodization[26,27] of an aluminum thin film under a constant current density. Figure 2A shows the voltage−time graph for first and second stage anodization, showing the progression of pore formation

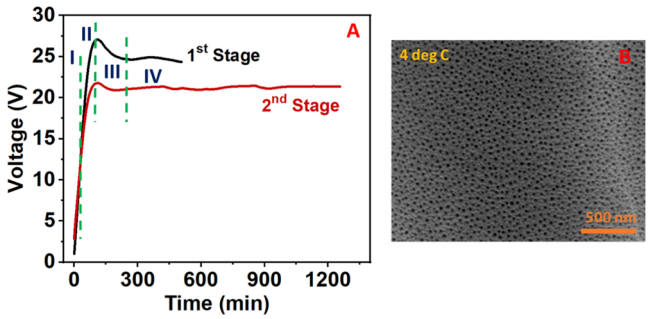

Figure 2. Voltage−time characteristics for first- and second stage anodization (A). SEM images of nanopores formed at the end of the first stage performed at 4 °C (B).

including (1) barrier oxide formation, (2) pore initiation, (3) pore propagation, and (4) steady-state pore growth.[6] During the second stage anodization, conversion of the aluminum film to alumina resulted in the transition of the substrate from opaque to optically transparent. Continuation of anodization beyond this transition resulted in a rapid voltage increase and damage to the ITO layer (Figure S1). Hence, second stage anodization was terminated before the onset of the rapid voltage increase to prepare NAA/ITO/glass electrodes. After anodizing, an etching step was used to remove barrier oxide at the pore bottom for the electrolyte to make contact with the underlying ITO layer. The anodization process was carried out at low temperatures, required to dissipate the excess heat generated during the process for ensuring regular pores.[8,12,28,29] The micrographs of the pores formed at 4 °C at the end of the first stage are shown in Figure 2B, indicating good quality pores, while the quality of pores formed at room temperature was poor (Figure S2A). Final pore diameters of around 50−60 nm were achieved after performing the etching step, as shown in the SEM image in Figure S2B in the Supporting Information.

The Al/ITO/glass substrates that were initially reflective and opaque turn transparent with a mild bluish hue (Figure 1B) as a result of anodization of aluminum to nanoporous alumina. Optical transmittance measurements were used to ascertain the presence of alumina nanochannels on the electrode, as shown

https://doi.org/10.1021/acsami.1c17243
ACS Appl. Mater. Interfaces 2022, 14, 150−158

in the Supporting Information (Figure S3). The transmittance for ITO/glass substrates is about 80%, which is reduced to 50% for anodized substrates. The NAA/ITO/glass electrodes are transparent and can be potentially used as both optical and electrochemical sensors.

For electrochemical sensing of the α-thrombin protein, the nanopores were modified with (3-aminopropyl)-trimethoxysilane (APTMS) and functionalized with TBA as a receptor using glutaraldehyde cross-linking.[30] The impedance response of NAA/ITO/glass for different etching times and chemical modification steps determined using EIS are shown in Figure 3. The impedance of the samples after the second stage anodization was very high (Figure 3a), indicating the presence of a barrier film at the pore bottom. Etching the film for 3−7.5 min decreased the impedance (Figure 3b−d) as a result of an increase in pore size and removal of the barrier layer. For sensing experiments, the etching time of the electrode was limited to 7.5 min to ensure dissolution of the pore bottom oxide layer and limit the increase in pore size, as the sensitivity of the biosensor is higher with lower pore diameters.[22] After APTMS−glutaraldehyde treatment, the substrate impedance increased, indicating surface chemical modification (Figure 3e), and decreased with the attachment of TBA (Figure 3f), indicating immobilization of negatively charged DNA on the alumina surface.[24]

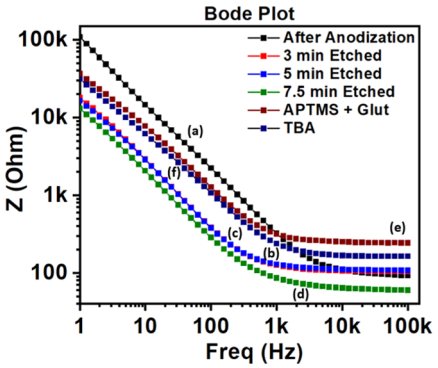

Figure 3. Electrochemical characterization of NAA/ITO/glass after second stage anodization (a), for various etching times (b−d), after APTMS + glutaraldehyde (e), and TBA (f).

2.2. Electrochemical Sensing of α-Thrombin. Nyquist plots obtained from the EIS of the TBA-functionalized electrodes exposed to different concentrations of α-thrombin are plotted in Figure 4. The increase in thrombin concentration in the electrolyte resulted in an increase in electrode impedance. Measured EIS data were fitted to a circuit model consisting of solution resistance (R_s) and two Randles circuits (with resistance and a constant phase element) in series corresponding to the pore (R_p, C_p) and the conductive ITO electrode (R_{ct}, C_{ct}) (Figure S4). NAA/ITO/glass electrodes are covered with an aptamer-functionalized nanochannel array, and the spatial nonuniformities in the anodized films result in frequency dispersion in the measured EIS response. Hence, constant phase elements (CPEs) are used in the circuit model instead of pure capacitive elements.[11,30−32] As we are interested in the processes happening in the nanopore due to the aptamer−protein binding, a change in R_p is taken as the sensor signal.

Figure 4B shows the plot of the normalized change in the fitted pore resistance with increasing concentrations of α-thrombin. The sensor showed an increase in resistance with α-thrombin but an insignificant impedance change was observed in the presence of γ-thrombin solutions. γ-Thrombin has a similar structure as α-thrombin but lacks the aptamer binding epitope[33] and hence constitutes an ideal negative control to confirm the specificity of the sensor response. Table 1 summarizes the signal obtained for different concentrations of α-thrombin and γ-thrombin relative to the noise measured for the sensor. The electrodes showed an exceptionally high response to α-thrombin with S/N ratios being at least 20 times higher in comparison to γ-thrombin for 2 nM protein concentration. The average relative standard deviation (RSD) for the sensing response is in the range of 9−18% (Table S1).

The curve of the normalized resistance change as a function of increasing α-thrombin concentration was approximated as the Langmuir isotherm, and the dissociation constant, K_D, for α-thrombin on TBA-functionalized pores was calculated to be around 1 nM. A similar range of K_D values have been reported in previous studies for TBA−α-thrombin systems employing nanoporous platforms.[25,34] The sensor showed a linear response ($R^2 \sim 0.97$) over an α-thrombin concentration change in the range of 0.01−2 nM with the lowest detection threshold of about 10 pM. As outlined in Tables S2 and S3, the fabricated label-free NAA/ITO/glass electrodes showed much higher responses compared to previously reported sensor formats[23,25,35] for thrombin detection while exhibiting comparable performance with respect to detection limits and dynamic ranges.

The binding of the target to the aptamer in the nanopore can modify ionic and mass transport through[4,35,36] (a) steric effects that result in the reduction of the pore diameter and (b)

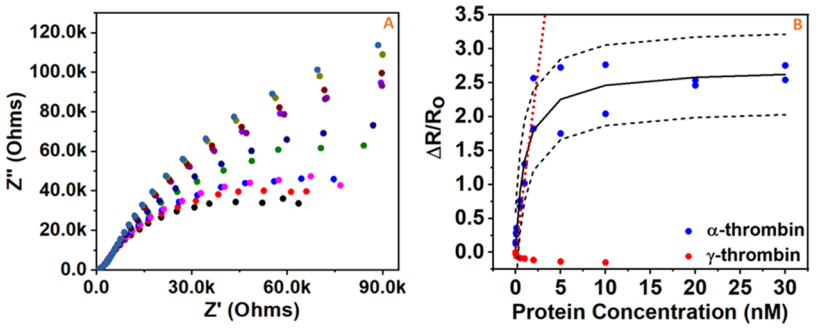

Figure 4. Nyquist plots showing variation in impedance with increasing concentrations of α-thrombin: 0−30 nM (A). Plot showing normalized pore resistance changes with α-thrombin and the specificity test with γ-thrombin (B).

https://doi.org/10.1021/acsami.1c17243
ACS Appl. Mater. Interfaces 2022, 14, 150−158

Table 1. S/N Ratios Obtained for Different Concentrations Calculated from the Averaged Signal (dR/R) Obtained with α-Thrombin and γ-Thrombin[a]

	signal$_{avg}$			S/N	
concentration (nM)	α-thrombin	γ-thrombin	noise$_{avg}$	α-thrombin	γ-thrombin
0.01	0.14	0.02	0.03	4.9	0.8
0.05	0.20	0.03		6.9	1.1
0.1	0.31	0.06		10.5	2.0
0.5	0.72	0.09		24.3	2.9
1	1.16	0.09		39.2	3.1
2	2.19	0.11		74.2	3.8
5	2.24	0.14		75.6	4.7
10	2.40	0.15		81.2	5.1
20	2.50			84.5	
30	2.65			89.5	

[a]Noise is averaged dR/R measured across TBA-functionalized NAA without introducing any protein.

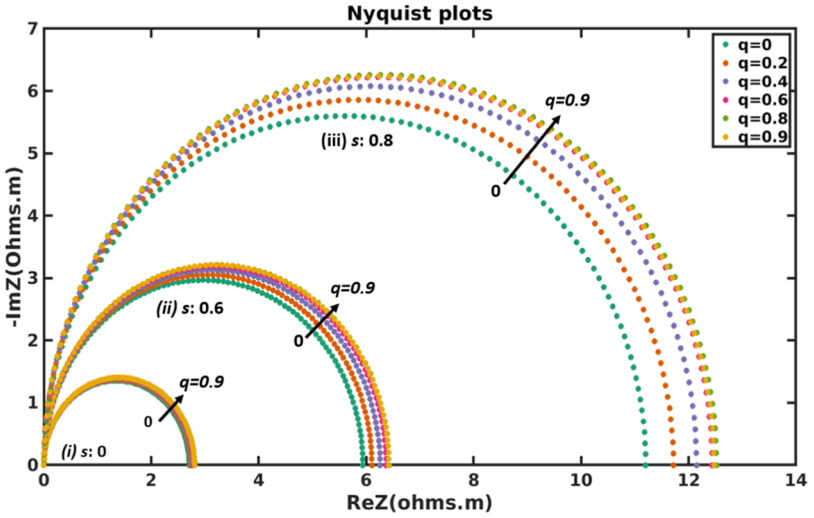

Figure 5. Nyquist plot predicted by computational EIS for varying q from 0 to 0.9 and s = 0, 0.6, and 0.8.

surface charge modulation due to quenching of negative charges on aptamer oligonucleotides. The hydrodynamic size of the TBA−thrombin complex is estimated to be between 70 and 100 nm (in a pH range of 7−8)[37] but the complex height on a gold surface was measured to be around 2−4 nm.[38] In the current work, the aptamer−protein complex formation inside the alumina nanopore may cause a reduction in the pore diameter of at least 20−40 nm[23] and can cause significant steric hindrance to ionic conduction in the nanopores. In contrast to this, for asymmetrically functionalized nanopores with the aptamer only covering the selected region at the entrance of the pore,[25,34] we observed that surface charge modulation dominated the sensor response and the pore resistance decreased upon binding to the target protein. The localized charge modulation only near the entrance of the nanopores due to binding increased the nanopore conductance significantly.

In the current sensor configuration, both steric and surface charge modulation may be responsible for the increase in pore resistance. Previously reported analytical equations[39,40] were used to predict the sensor response due to steric and charge effects caused by aptamer/thrombin binding. Considering steric effects alone, the dR/R change on aptamer/thrombin binding was approximately calculated to be about 1.7 assuming that the pore diameter reduced from initial 50 to 10 nm. The binding of α-thrombin can cause a net charge modulation of about 11−12 mC/m^2.[41] Therefore, considering the surface charge density to change from −50 to −30 mC/m^2 on aptamer/thrombin binding, a dR/R of 0.085 was obtained. The response seen in the experiments is significantly larger than those calculated by considering steric or charge effects alone and may be due to the synergistic combination of reduction in the pore diameter and quenching of surface charges. Also, the equations derived for pore conductance describe experimental steady-state conductance measurements[39,40] and may not capture the frequency-dependent impedance response obtained using experimental techniques such as EIS. To quantify the relative contributions of steric and charge phenomena to the frequency-dependent sensor response, the "computational EIS" tool is used to compute EIS spectra for direct comparison with the experiments.

2.3. Computational Modeling of the Mechanism Underlying the Sensor Response. The computational EIS method predicts the frequency response of the system based on transient electric currents due to a step change in the voltage.[34] Transient currents were calculated using a finite element solution[42] of Poisson−Nernst−Planck equations. To understand the mechanism of aptamer−protein interactions in nanoporous systems, we studied the transient ionic transport phenomena occurring in a single nanopore in contact with the conductive electrode on one end and the reservoir on the other end, mimicking the NAA/ITO/glass sensor configuration

https://doi.org/10.1021/acsami.1c17243
ACS Appl. Mater. Interfaces 2022, 14, 150−158

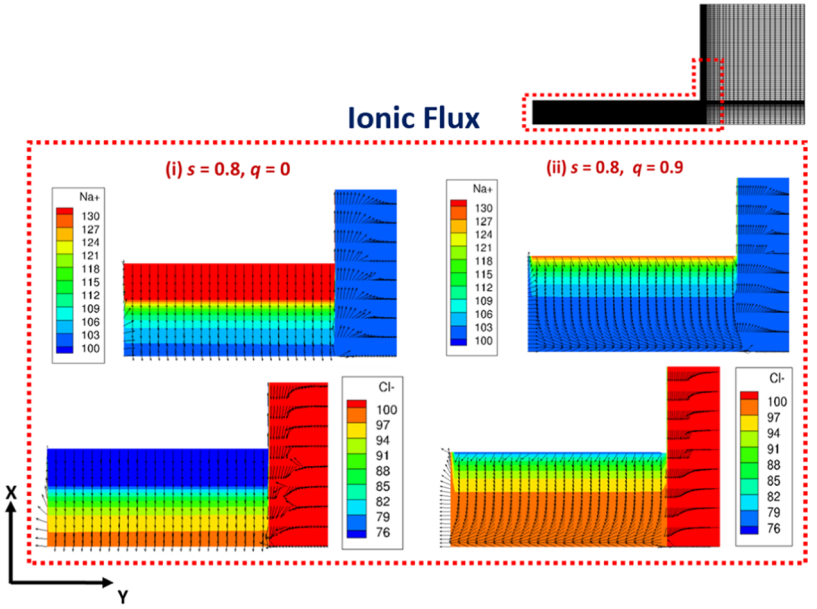

Figure 6. Concentration distribution and the directions of Na^+ and Cl^- fluxes for (i) $s = 0.8$, $q = 0$ and (ii) $s = 0.8$, $q = 0.9$ in the region close to the nanochannel (concentrations are in mM).

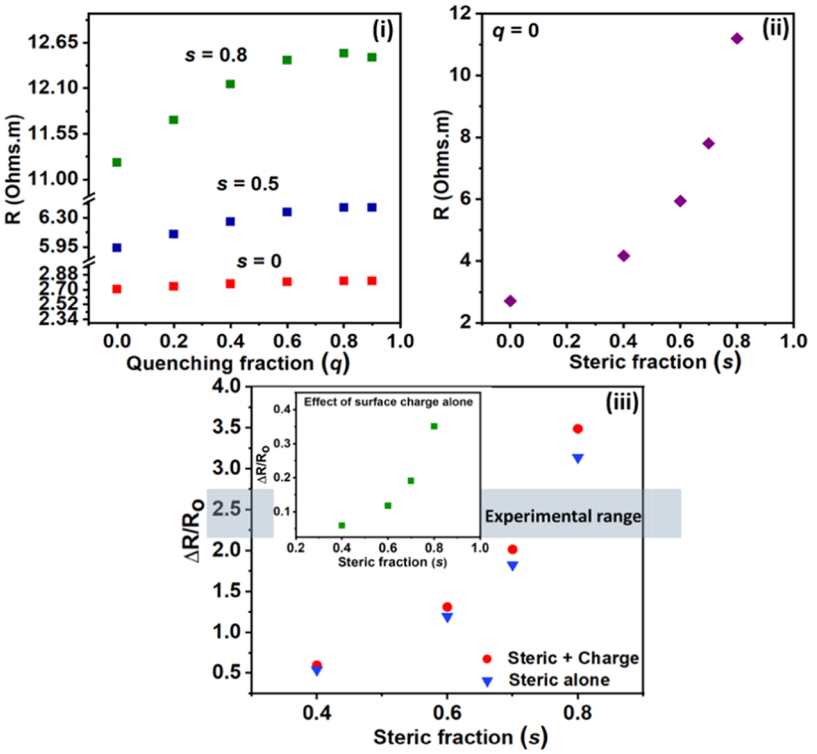

Figure 7. Plot showing the pore resistance variations with q for $s = 0$, 0.6, and 0.8 (i), pore resistance versus s (ii), and the plot showing the normalized pore resistance change with s for steric effects alone versus steric and charge effects together. The band represents the experimentally determined maximum sensor signal (iii). The inset shows the effect of the charge effect alone for different s values.

(Figure 1E). The influence of steric and charge modulation on the pore impedance was studied by introducing the parameters steric (s) and quenching (q) fractions, respectively, which are defined as

$$d_{\text{aptamer/protein}} = (1 - s)d_{\text{aptamer}} \quad (1)$$

$$\sigma_{\text{aptamer/protein}} = (1 - q)\sigma_{\text{aptamer}} \quad (2)$$

where $d_{\text{aptamer/protein}}$ and $\sigma_{\text{aptamer/protein}}$ are the diameter and surface charge of the aptamer−protein complex-covered surface, respectively, while d_{aptamer} and σ_{aptamer} are the diameter and surface charge of the aptamer-functionalized nanochannel, respectively. The steric effects of the aptamer−protein binding were investigated by varying the pore diameter from the initial d_{aptamer} of 50 nm ($s = 0$) to the final $d_{\text{aptamer/protein}}$ of 10 nm ($s = 0.8$). The surface charge density was varied from the initial

https://doi.org/10.1021/acsami.1c17243
ACS Appl. Mater. Interfaces 2022, 14, 150−158

$\sigma_{aptamer}$ of −50 mC/m^2 (q = 0) to the final $\sigma_{aptamer/protein}$ value of −5 mC/m^2 (q = 0.9) to account for the charge modulation caused by binding to the positively charged protein. The initial charge density was computed based on the aptamer length of 50 nucleotides and a grafting density of about 10^{12} chains/cm^2 at 100 mM salt concentration.[41]

Figure 5 shows the Nyquist plots predicted from the computational EIS model for three cases of s: (i) s = 0 (50 nm), (ii) s = 0.6 (20 nm), and (iii) s = 0.8 (10 nm), and for each case of s, q was varied from 0 (−50 mC/m^2) to 0.9 (−5 mC/m^2). For all cases of s, the impedance showed an increase as q varied from 0 to 0.9, and this change in impedance was higher as the s value increased from 0 (50 nm) to 0.8 (10 nm). Therefore, the data predicted from the computational model suggest that as the protein binds to the aptamer, both the diameter reduction and the surface charge quenching of the nanopore contribute to the increase in the pore resistance observed in the experiments.

To understand the effect of charge on impedance behavior, the concentration distribution and the directions of cation and anion fluxes were investigated for a pore diameter of 10 nm. Aptamer-functionalized nanopores acquire a high negative charge of −50 mC/m^2 (q = 0). When a positively charged protein binds to the aptamer, which neutralizes the negative surface charge, it decreases the pore charge to −5 mC/m^2 (q = 0.9). Hence, two charge conditions were studied, i.e., (i) s = 0.8, q = 0 (steric alone) and (ii) s = 0.8, q = 0.9 (both steric and charge, Figure 6). In case (i), due to the high surface charge of the nanopore, Na^+ ions get enriched and Cl^- ions get depleted close to the nanopore walls almost by 10 times. The high influx of Na^+ ions into the nanopore also increases the amount of Cl^- transport flux to maintain electroneutrality, resulting in enhanced ionic transport (Figure 6i). In case (ii), the enrichment of Na^+ and depletion of Cl^- ions are only about 1.3 times due to lower pore surface charge. Therefore, when the protein binds to the aptamer, the surface charge quenching results in lower ionic fluxes of Na^+ and Cl^-, increasing the impedance across the nanopore.

Computation of flux components shows that there is a build-up of X-direction flux with changes in the pore surface charge. This effect is more apparent in 10 nm pores (s = 0.8) where the X-direction flux extends into the pore center compared to 50 nm pores (s = 0, Figure S6). Hence, the effect of charge modulation on impedance is more significant in lower pore diameters. The increase in impedance is expected to be greater for s = 0.8, q = 0.9 when both steric and charge effects are acting together compared to steric effects alone, i.e., s = 0.8, q = 0, as a higher surface charge is associated with high pore conductivity. The quantitative changes in impedance can be inferred from Figure 7, where the extracted pore resistance is plotted against (i) q for s = 0 (50 nm), 0.6 (20 nm), 0.8 (10 nm) considering the charge effect alone and (ii) s for q = 0 (−50 mC/m^2) considering steric effects alone.

To compare trends between the computed sensor response with experimental measurements, the normalized pore resistance changes (normalized with respect to R_0 (q = 0)) are plotted against s (Figure 7iii) comparing steric effects alone versus combined steric and charge effects. The thrombin/aptamer complex formation is expected to result in a change of q from 0 (−50 mC/m^2) to 0.4 (−30 mC/m^2). Hence, the pore resistance changes with/without charge are computed as shown in eqs 3 and 4, respectively. The effect of charge alone computed by subtracting $\Delta R/R_0$ for steric effects alone from combined steric and charge effects for different s values is shown in the inset. It can be inferred from the plot that for lower s (0.4/30 nm), the effect of charge modulation is not significant, i.e., less than 10%. The role of charge starts to become important for s values of 0.6 and above.

$$\Delta R/R_0 = \frac{R(s = 0.4, 0.6, 0.7, 0.8), q = 0.4) - R(s = 0.0, q = 0)}{R(s = 0.0, q = 0)} \quad (3)$$

$$\Delta R/R_0 = \frac{R(s = 0.4, 0.6, 0.7, 0.8), q = 0) - R(s = 0.0, q = 0)}{R(s = 0.0, q = 0)} \quad (4)$$

Fitting the response obtained with both steric and charge effects (Figure S9) and taking $\Delta R/R_0$ as 2.5, deduced from the experiments (Figure 4B), s can be predicted to be about 0.74, which corresponds to a pore diameter of 13 nm. Hence, binding of thrombin may result in a reduction in the pore diameter by 37 nm. The results from the computational EIS may be used to estimate the relative contributions of steric hindrance and charge modulation to the sensor response. The current sensor configuration with a nominal pore diameter of 50 nm can achieve high sensitivity, but reducing the pore size of nanoporous alumina may result in further improvement of the sensor response and sensitivity. The sensor fabrication process involving anodization of aluminum and etching to remove the barrier oxide at the pore bottom may be optimized to achieve pores of smaller diameters.

3. CONCLUSIONS

We report fabrication and characterization of a nanoporous biosensor based on an anodized alumina film on an ITO/glass substrate. A thrombin aptamer-functionalized alumina/ITO/glass sensor exhibits a very high S/N ratio of 90 and a detection threshold of 10 pM for α-thrombin. In addition, a negligible response on exposure to γ-thrombin was observed, indicating the specificity of the aptamer-functionalized sensor. Our experimental and computational results show that the high sensitivity and specificity of the biosensor are due to the combined influence of steric and surface charge changes during aptamer−protein binding on the ionic conduction in the closed pore configuration. The computational results indicate that the sensitivity can be improved through further reduction in the pore diameter. The aptamer-functionalized alumina/ITO/glass sensors are easy to fabricate, provide a highly specific and sensitive response, and are amenable for integration with impedance monitoring circuits to implement point-of-care sensing devices.

4. MATERIALS AND METHODS

4.1. Reagents and Materials. Reagents for two-stage anodization—sulfuric acid (95−98%), phosphoric acid (85%), and chromic acid—were obtained from Fisher Scientific. ITO/glass substrates, 2% 3-aminopropyltrimethoxy silane (APTMS), ethanolamine, and 5% glutaraldehyde were obtained from Sigma-Aldrich. Aluminum and titanium 99.999% pure targets were obtained from Kurt Lesker for coating the ITO/glass substrate. Aminated-TBA was purchased from Integrated DNA Technologies (IDT) with the sequence 5′-/5AmMC6/GCCTTAACTGTAGTACTGGTGAAATTGCTGC-CATT**GGTTGGTGTGGTTGG**-3′. Proteins used in experiments

https://doi.org/10.1021/acsami.1c17243
ACS Appl. Mater. Interfaces 2022, 14, 150−158

(human α-thrombin and γ-thrombin) were purchased from Thermo Fisher Scientific. All experiments were performed in a buffer solution consisting of 137 mM NaCl, 2.7 mM KCl, 10 mM Na_2HPO_4, and 2 mM KH_2PO_4 pH 7.4 at room temperature. All of the salts used for electrolyte were purchased from Sigma-Aldrich, and the solutions were prepared with distilled deionized water (ddH_2O) obtained from the Corning Mega Pure system.

4.2. Fabrication of NAA/ITO/Glass Substrates. NAA/ITO/glass electrodes were fabricated using galvanostatic two-stage anodization (Figure 1A,B). ITO/glass substrates were first coated with aluminum to a thickness of 1 μm using the E-beam evaporation method (Temescal BJT-1800) with 10 nm titanium as an adhesion layer. First and second stage anodization was carried out in 0.45 M sulfuric acid at a current density of 2.5 mA/cm^2 and etching in a mixture of 6% phosphoric acid and 1.8% chromic acid.

4.3. Aptamer Attachment to NAA/ITO/Glass Substrates. The procedure for the attachment of TBA to NAA/ITO/glass is shown in Figure 1C. NAA surfaces were silanized by first using APTMS for 1 h, washing with ethanol, and then baking for 3 h at 120 °C. Then, the surfaces were treated with glutaraldehyde for 1 h, which acts as a cross-linking agent, and rinsed with ddH_2O. Aminated-TBA was stored at 100 μM in buffer solutions at −20 °C. Before each experiment, TBA was diluted to 1 μM concentration in the buffer and annealed by first heating to 95 °C. Subsequently, 5 mM $MgCl_2$ was added to the heated solution and the solution was cooled down to room temperature (RT) slowly over a period of at least 45 min. Then, the functionalized NAA/ITO/glass electrodes were incubated with aminated-TBA overnight at room temperature, followed by treatment with 100 mM ethanolamine for 40 min, which acts as a blocking agent. After each substrate preparation step, the electrodes were rinsed multiple times with PBS.

4.4. Characterization of the NAA/ITO/Glass Biosensor. Optical characterization of the NAA/ITO/glass substrate was carried out using UV−vis spectroscopy (Agilent 8453 UV−vis). All electrochemical measurements were carried out using a Gamry potentiostat/galvanostat/ZRA (Model, REF 600) in a three-electrode configuration with NAA/ITO/glass as the working electrode, a silver/silver chloride wire as the reference electrode, and a platinum wire as the counter electrode in PBS solution, pH 7.4. A custom-made Teflon cell was used to conduct the experiments (Figure 1D). For all sensing experiments, aptamer-coated substrates were mounted in the cells and exposed to the desired concentration of α-thrombin as an analyte and γ-thrombin as negative control solutions. The transmembrane impedance of the substrate exposed to protein solutions was measured over a frequency range of 0.1 Hz−100 kHz with an AC perturbation of 5 mV. EIS measurements were fitted to an equivalent circuit model using Gamry analyst software. Changes in transmembrane impedance were monitored as a function of protein concentration to obtain a calibration curve for NAA/ITO/glass sensors.

4.5. Computational EIS Modeling. The NAA/ITO/glass substrate response was modeled using a single nanopore with a closed configuration, as shown in Figure 1E. Numerical models of nanopores with a length of 1 μm and diameters of 10, 15, 20, 30, and 50 nm were analyzed to investigate the influence of the aspect ratio on the sensing response. The right boundary of the nanopores was grounded, and a step voltage of 5 mV was applied at the left boundary. The surface charge $\sigma_{aptamer}$ = −50 mC/m^2 was applied to the nanopore walls to model a TBA self-assembled monolayer. The binding of positively charged α-thrombin on the TBA-covered surface was expected to quench the TBA surface charges. Hence, specific binding of α thrombin and the aptamer was modeled through a surface charge reduction to −5 mC/m^2. The finite element solution of the Poisson−Nernst−Planck equations (shown below) was used to determine the ionic currents in the pore due to a step voltage of 5 mV applied at the left boundary.[34,42]

$$\frac{\partial c_i}{\partial t} + \nabla\cdot\left[uc_i - D_i\nabla c_i - D_i\frac{z_iF}{RT}c_i\nabla\phi\right] = 0 \quad (5)$$

$$-\epsilon\nabla^2\phi = F\sum c_iz_i \quad (6)$$

where c_i and ϕ are species concentration and potential, respectively. D_i is the diffusion coefficient, z_i is the charge valence, F is the Faraday number, R is the gas constant, T is the temperature, and ε_0 and ε_r are the absolute and relative permittivities, respectively. The mesh convergence studies of the computational code are described in the Supporting Information. The "computational EIS" of the membrane was computed from the fast Fourier transform (FFT) of the computed ionic current according to the procedures described previously.[34,42]

■ ASSOCIATED CONTENT

Supporting Information

The Supporting Information is available free of charge at https://pubs.acs.org/doi/10.1021/acsami.1c17243.

Plot showing $I-V$ characteristics for second stage anodization (Figure S1); SEM images of nanopores formed at the end of the first stage performed at (A) room temperature and (B) at the end of the second stage and etching (Figure S2); optical transmittance characterization (Figure S3); circuit model used for the analysis of EIS data (Figure S4); bode plots showing variation in impedance with increasing concentrations of α-thrombin: 0−30 nM (Figure S5); averaged signal (dR/R) and RSD % obtained with α-thrombin (Table S1); comparison table of current sensor performance with previously reported NAA sensors (Table S2); comparison table of current sensor performance with previously reported thrombin aptamer-based sensors (Table S3); concentration distribution and the directions of Na^+ and Cl^- fluxes for (i) s = 0, q = 0 and (ii) s = 0, q = 0.9 in the region close to the nanochannel (concentrations are in mM) (Figure S6); concentration distribution and the directions of Na^+ and Cl^- fluxes for (i) s = 0 and low positive, σ = 1 mC/m^2 (Figure S7); predicted Nyquist plot from computational EIS with/without TBA (Figure S8); computed pore resistance versus s and fit used to compute the pore diameter (Figure S9); and mesh convergence study (Figure S10) (PDF)

■ AUTHOR INFORMATION

Corresponding Authors

Baskar Ganapathysubramanian − *Department of Mechanical Engineering, Iowa State University, Ames, Iowa 50011, United States*; Email: baskarg@iastate.edu

Pranav Shrotriya − *Department of Mechanical Engineering, Iowa State University, Ames, Iowa 50011, United States*; orcid.org/0000-0001-9263-4892; Email: shrotriy@iastate.edu

Author

Sivaranjani Devarakonda − *Department of Mechanical Engineering, Iowa State University, Ames, Iowa 50011, United States*

Complete contact information is available at: https://pubs.acs.org/10.1021/acsami.1c17243

Author Contributions

S.D. and P.S. devised the problem statement. S.D. conducted the literature review, experiments, and computational

validation. S.D., P.S., and B.G. wrote, reviewed, and edited the manuscript.

Notes

The authors declare no competing financial interest.

■ ACKNOWLEDGMENTS

Research reported in this publication was partially supported by the NIDDK Institute of the National Institutes of Health under award number 5R44DK098031. This work was partially supported by the U.S. Department of Energy (DOE), Office of Biological and Environmental Research, Biological Systems Science Division under FWP No. AL-18-380-055 to the Ames Laboratory. The Ames Laboratory is operated for the U.S. Department of Energy by Iowa State University under contract number DE-AC02-07CH11358. Computing support from TG-CTS110007 is acknowledged. Support from the ISU Plant Science Institute is acknowledged. Helpful suggestions and technical discussions with Prof. Marit Nilsen-Hamilton and Dr. Sungu Kim are gratefully acknowledged.

■ REFERENCES

(1) Gyurcsányi, R. E. Chemically-Modified Nanopores for Sensing. *TrAC, Trends Anal. Chem.* **2008**, *27*, 627−639.
(2) Majd, S.; Yusko, E. C.; Billeh, Y. N.; Macrae, M. X.; Yang, J.; Mayer, M. Applications of Biological Pores in Nanomedicine, Sensing, and Nanoelectronics. *Curr. Opin. Biotechnol.* **2010**, *21*, 439−476.
(3) Chen, Y.; Liu, B.; Chen, Z.; Zuo, X. Innovative Electrochemical Sensor Using TiO2 Nanomaterials to Detect Phosphopeptides. *Anal. Chem.* **2021**, *93*, 10635−10643.
(4) Ali, M.; Nasir, S.; Ensinger, W. Bioconjugation-Induced Ionic Current Rectification in Aptamer-Modified Single Cylindrical Nanopores. *Chem. Commun.* **2015**, *51*, 3454−3457.
(5) Lin, X.; Ivanov, A. P.; Edel, J. B. Selective single molecule nanopore sensing of proteins using DNA Aptamer-Functionalised Gold Nanoparticles. *Chem. Sci.* **2017**, *8*, 3905−3912.
(6) Lee, W.; Park, S.-J. Porous Anodic Aluminum Oxide: Anodization and Templated Synthesis of Functional Nanostructures. *Chem. Rev.* **2014**, *114*, 7487−7556.
(7) Santos, A.; Kumeria, T.; Losic, D. Nanoporous Anodic Aluminum Oxide for Chemical Sensing and Biosensors. *TrAC, Trends Anal. Chem.* **2013**, *44*, 25−38.
(8) Chu, S. Z.; Wada, K.; Inoue, S.; Todoroki, S. Formation and Microstructures of Anodic Alumina Films from Aluminum Sputtered on Glass Substrate. *J. Electrochem. Soc.* **2002**, *149*, B321.
(9) Chung, C. K.; Liao, M. W.; Khor, O. K.; Chang, H. C. Enhancement of Pore Size Distribution in One-step Hybrid Pulse Anodization of Aluminum Thin Films Sputtered on Si Substrates. *Thin Solid Films* **2013**, *544*, 374−379.
(10) Hong, C., Fang, W., Shew, B. Flexible nanoporous anodic aluminum oxide(np-AAO) template coated with self-assembled Au nanocrown array for nanophotonic switching.*International Conference on Optical MEMS and Nanophotonics (OMN)*, 2013, pp 135−136, DOI: 10.1109/OMN.2013.6659096.
(11) Nguyen, B. T. T.; Peh, A. E. K.; Chee, C. Y. L.; Fink, K.; Chow, V. T. K.; Ng, M. M. L.; Toh, C.-S. Electrochemical Impedance Spectroscopy Characterization of Nanoporous Alumina Dengue Virus Biosensor. *Bioelectrochemistry* **2012**, *88*, 15−21.
(12) Foong, T. R. B.; Sellinger, A.; Hu, X. Origin of the Bottlenecks in Preparing Anodized Aluminum Oxide (AAO) Templates on ITO Glass. *ACS Nano* **2008**, *2*, 2250−2256.
(13) Teh, L. K.; Furin, V.; Martucci, A.; Guglielmi, M.; Wong, C. C.; Romanato, F. Electrodeposition of CdSe on Nanopatterned Pillar Arrays for Photonic and Photovoltaic Applications. *Thin Solid Films* **2007**, *515*, 5787−5791.
(14) Zhou, Q.; Lin, Y.; Lin, Y.; Wei, Q.; Chen, G.; Tang, D. Highly Sensitive Electrochemical Sensing Platform for Lead Ion Based on Synergetic Catalysis of DNAzyme and Au−Pd Porous Bimetallic Nanostructures. *Biosens. Bioelectron.* **2016**, *78*, 236−243.
(15) Lv, S.; Zhang, K.; Zhu, L.; Tang, D.; Niessner, R.; Knopp, D. H2-Based Electrochemical Biosensor with Pd Nanowires@ZIF-67 Molecular Sieve Bilayered Sensing Interface for Immunoassay. *Anal. Chem.* **2019**, *91*, 12055−12062.
(16) Shu, J.; Qiu, Z.; Tang, D. Self-Referenced Smartphone Imaging for Visual Screening of H2S Using CuxO-Polypyrrole Conductive Aerogel Doped with Graphene Oxide Framework. *Anal. Chem.* **2018**, *90*, 9691−9694.
(17) Vlassiouk, I.; Kozel, T. R.; Siwy, Z. S. Biosensing with Nanofluidic Diodes. *J. Am. Chem. Soc.* **2009**, *131*, 8211−8220.
(18) Plett, T. S.; Cai, W.; Le Thai, M.; Vlassiouk, I. V.; Penner, R. M.; Siwy, Z. S. Solid-State Ionic Diodes Demonstrated in Conical Nanopores. *J. Phys. Chem. C* **2017**, *121*, 6170−6176.
(19) Rosentsvit, L.; Wang, W.; Schiffbauer, J.; Chang, H.-C.; Yossifon, G. Ion Current Rectification in Funnel-shaped Nanochannels: Hysteresis and Inversion Effects. *J. Chem. Phys.* **2015**, *143*, No. 224706.
(20) Li, X.; Zhai, T.; Gao, P.; Cheng, H.; Hou, R.; Lou, X.; Xia, F. Role of Outer Surface Probes for Regulating Ion Gating of Nanochannels. *Nat. Commun.* **2018**, *9*, No. 40.
(21) Vlassiouk, I.; Takmakov, P.; Smirnov, S. Sensing DNA Hybridization via Ionic Conductance through a Nanoporous Electrode. *Langmuir* **2005**, *21*, 4776−4778.
(22) Kant, K.; Yu, J.; Priest, C.; Shapter, J. G.; Losic, D. Impedance Nanopore Biosensor: Influence of Pore Dimensions on Biosensing Performance. *Analyst* **2014**, *139*, 1134−1140.
(23) Zhao, X.-P.; Cao, J.; Nie, X.-G.; Wang, S.-S.; Wang, C.; Xia, X.-H. Label-free Monitoring of the Thrombin-Aptamer Recognition Reaction Using an Array of Nanochannels Coupled with Electrochemical Detection. *Electrochem. Commun.* **2017**, *81*, 5−9.
(24) Wang, X.; Smirnov, S. Label-free DNA Sensor Based on Surface Charge Modulated Ionic conductance. *ACS Nano* **2009**, *3*, 1004−1010.
(25) Gosai, A.; Hau Yeah, B. S.; Nilsen-Hamilton, M.; Shrotriya, P. Label-free Thrombin Detection in Presence of High Concentration of Albumin Using an Aptamer-Functionalized Nanoporous Membrane. *Biosens. Bioelectron.* **2019**, *126*, 88−95.
(26) Lin, Y.; Lin, Q.; Liu, X.; Gao, Y.; He, J.; Wang, W.; Fan, Z. A Highly Controllable Electrochemical Anodization Process to Fabricate Porous Anodic Aluminum Oxide Membranes. *Nanoscale Res. Lett.* **2015**, *10*, No. 495.
(27) Li, Y.; Chen, Y.; Qiu, M.; Yu, H.; Zhang, X.; Sun, X. W.; Chen, R. Preparation of Aluminum Nanomesh Thin Films from an Anodic Aluminum Oxide Template as Transparent Conductive Electrodes. *Sci. Rep.* **2016**, *6*, No. 20114.
(28) Liu, S.; Xiong, Z.; Zhu, C.; Li, M.; Zheng, M.; Shen, W. Fast Anodization Fabrication of AAO and Barrier Perforation Process on ITO Glass. *Nanoscale Res. Lett.* **2014**, *9*, No. 159.
(29) Hill, J. J.; Haller, K.; Ziegler, K. J. Direct Fabrication of High-Aspect Ratio Anodic Aluminum Oxide with Continuous Pores on Conductive Glass. *J. Electrochem. Soc.* **2011**, *158*, E1.
(30) Deng, J.; Toh, C.-S. Impedimetric DNA Biosensor Based on a Nanoporous Alumina Membrane for the Detection of the Specific Oligonucleotide Sequence of Dengue Virus. *Sensors* **2013**, *13*, 7774−7785.
(31) Römer, W.; Steinem, C. Impedance Analysis and Single-Channel Recordings on Nano-Black Lipid Membranes Based on Porous Alumina. *Biophys. J.* **2004**, *86*, 955−965.
(32) Sharma, G.; Pishko, M. V.; Grimes, C. A. Fabrication of Metallic Nanowire Arrays by Electrodeposition into Nanoporous Alumina Membranes: Effect of Barrier Layer. *J. Mater. Sci.* **2007**, *42*, 4738−4744.
(33) Deng, B.; Lin, Y.; Wang, C.; Li, F.; Wang, Z.; Zhang, H.; Li, X.-F.; Le, X. C. Aptamer Binding Assays for Proteins: The Thrombin Example−A Review. *Anal. Chim. Acta* **2014**, *837*, 1−15.

(34) Devarakonda, S.; Kim, S.; Ganapathysubramanian, B.; Shrotriya, P. Designing Asymmetrically Modified Nanochannel Sensors Using Virtual EIS. *Electrochim. Acta* **2021**, No. 139694.
(35) de la Escosura-Muñiz, A.; Chunglok, W.; Surareungchai, W.; Merkoçi, A. Nanochannels for Diagnostic of Thrombin-Related Diseases in Human Blood. *Biosens. Bioelectron.* **2013**, *40*, 24−31.
(36) Li, S.-J.; Xia, N.; Yuan, B.-Q.; Du, W.-M.; Sun, Z.-F.; Zhou, B.-B. A Novel DNA Sensor Using a Sandwich Format by Electrochemical Measurement of Marker Ion Fluxes across Nanoporous Alumina Membrane. *Electrochim. Acta* **2015**, *159*, 234−241.
(37) Tan, S. Y.; Acquah, C.; Tan, S. Y.; Ongkudon, C. M.; Danquah, M. K. Characterisation of Charge Distribution and Stability of Aptamer-Thrombin Binding Interaction. *Process Biochem.* **2017**, *60*, 42−51.
(38) Ma, X.; Gosai, A.; Balasubramanian, G.; Shrotriya, P. Aptamer Based Electrostatic-Stimuli Responsive Surfaces for On-Demand Binding/Unbinding of a Specific Ligand. *J. Mater. Chem. B* **2017**, *5*, 3675−3685.
(39) Frament, C. M.; Dwyer, J. R. Conductance-Based Determination of Solid-State Nanopore Size and Shape: An Exploration of Performance Limits. *J. Phys. Chem. C* **2012**, *116*, 23315−23321.
(40) Lee, C.; Joly, L.; Siria, A.; Biance, A.-L.; Fulcrand, R.; Bocquet, L. Large Apparent Electric Size of Solid-State Nanopores Due to Spatially Extended Surface Conduction. *Nano Lett.* **2012**, *12*, 4037−4044.
(41) Stachowiak, J. C.; Yue, M.; Castelino, K.; Chakraborty, A.; Majumdar, A. Chemomechanics of Surface Stresses Induced by DNA Hybridization. *Langmuir* **2006**, *22*, 263−268.
(42) Kim, S.; Anand, R. K.; Ganapathysubramanian, B. Modeling Electrochemical Systems with Weakly Imposed Dirichlet Boundary Conditions. 2020, arXiv:2010.08778. arXiv.org e-Print archive. https://arxiv.org/abs/2010.08778 (accessed Oct 17, 2020).

https://doi.org/10.1021/acsami.1c17243
ACS Appl. Mater. Interfaces 2022, 14, 150−158